Materials Today Bio 23 (2023) 100881

Contents lists available at ScienceDirect

Materials Today Bio

journal homepage: www.journals.elsevier.com/materials-today-bio

Sprayable Ti_3C_2 MXene hydrogel for wound healing and drug release system

Hyeongtaek Park [a,1], Jeong-Uk Kim [b,1], Soojin Kim [a], Nathaniel S. Hwang [b,c,d,**], Hwan D. Kim [a,e,f,*]

[a] Department of IT Convergence (BK21 FOUR), Korea National University of Transportation, Chungju, 27469, Republic of Korea
[b] School of Chemical and Biological Engineering, Institute of Chemical Process, Seoul National University, Seoul, 08826, Republic of Korea
[c] BioMax/N-Bio Institute, Seoul National University, Seoul, 08826, Republic of Korea
[d] Institute of Engineering Research, Seoul National University, Seoul, 08826, Republic of Korea
[e] Department of Polymer Science and Engineering, Korea National University of Transportation, Chungju, 27469, Republic of Korea
[f] Department of Biomedical Engineering, Korea National University of Transportation, Chungju, 27469, Republic of Korea

ARTICLE INFO

Keywords:
Ti_3C_2 MXene
Drug delivery
Antibacterial
Wound healing
Sprayable hydrogel

ABSTRACT

Wound healing is a critical process that facilitates the body's recovery from injuries and helps prevent infections, thereby maintaining overall tissue and organ functionality. However, delayed wound healing owing to various factors can lead to bacterial infections and secondary complications. In this study, a ciprofloxacin (CIP)-loaded MXene/sodium alginate (SA) hydrogel was fabricated to inhibit bacterial infections and enhance wound healing. The hydrogel was formulated in a sprayable state by blending CIP-loaded MXene (CIP-MX) with SA. This hydrogel was found to exhibit excellent photothermal conversion capability and biocompatibility under near-infrared (NIR) irradiation. In addition, the hydrogel enabled controlled drug release based on NIR irradiation, ultimately enabling improved antibacterial activity. Based on the *in vitro* and *in vivo* experiments, the CIP-loaded MXene/SA hydrogel (CIP-MX@Gel) accelerated wound healing. Overall, the CIP-MX@Gel has excellent potential as an effective wound healing material.

1. Introduction

The remarkable capacity of the human body to heal wounds is a complex and vital process that is essential for preserving tissue function and safeguarding against infections and environmental damage [1–3]. Despite the inherent self-healing capabilities of the skin, cutaneous injuries, particularly persistent wounds and burns, require extensive and prolonged medical attention, imposing a substantial financial burden on global healthcare systems [4,5]. This delayed wound healing increases the risk of complications, notably infections [6,7]. Accordingly, researchers are actively exploring various techniques to enhance wound healing and prevent accompanying ailments.

Recent developments in biomedical engineering and materials science have led to innovative wound-healing approaches, such as the utilization of biomaterials and medication delivery systems [8,9]. Notably, hydrogels and dressings are examples of biomaterials that can accelerate tissue regeneration and expedite wound healing [10,11]. High moisture content, softness, and biocompatibility are only few of the distinctive physicochemical characteristics of hydrogels with three-dimensional (3D) cross-linked polymer networks. Furthermore, compounds containing growth factors and antimicrobials can be added to the hydrogels to accelerate healing. Sodium alginate (SA) hydrogels provide an environment conducive to cellular proliferation and migration during the intricate wound healing process. The remarkable biocompatibility and water retention capabilities of this hydrogel are pivotal for fostering essential cellular activities. Moreover, the pliable and supple attributes of this hydrogel ingeniously mimic the intricate architecture of the extracellular matrix (ECM), offering a mechanical scaffold that bolsters tissue regeneration and imparts comfort [12,13]. However, the use of SA in isolation, despite creating a nurturing milieu

* Corresponding author. Department of Polymer Science and Engineering Korea National University of Transportation 50 Daehak-ro, Chungju, 27469, Republic of Korea.
** Corresponding author. School of Chemical and Biological Engineering Seoul National University Seoul, 08826, Republic of Korea.
E-mail addresses: nshwang@snu.ac.kr (N.S. Hwang), hdkim@ut.ac.kr (H.D. Kim).
[1] These authors contributed equally to this work.

https://doi.org/10.1016/j.mtbio.2023.100881
Received 16 September 2023; Received in revised form 16 November 2023; Accepted 22 November 2023
Available online 28 November 2023

for cellular functions during wound healing, is limited by its inherent lack of antibacterial properties, rendering the wound vulnerable to potential infections [14]. Furthermore, controlling the release kinetics of growth factors and antimicrobials from hydrogels can be difficult, and these limitations may limit the results in the wound healing process. Accordingly, innovative strategies are required to improve the functionality of hydrogels and solve specific problems.

MXenes are promising 2D nanomaterials with potential applications in various biomedical fields [15,16]. This nanomaterial is typically produced by selective etching of the MAX phase, a transition metal carbide, or nitride. MXenes possess surface functional groups, such as hydroxyl (-OH) or oxygen (-O) groups, which contribute to their hydrophilic properties. In addition, the structure of MXene enables high electrical conductivity, excellent mechanical strength, biocompatibility, and tunable surface chemistry. These inherent properties make MXenes attractive candidates for diverse applications, including drug delivery, biosensing, tissue engineering, and wound healing. The high surface area of MXenes facilitates the efficient loading of therapeutic molecules, such as growth factors and antibiotics, affording control over the release kinetics and ultimately promoting effective wound healing. Moreover, the remarkable photothermal conversion ability of MXenes enables spatial and temporal control of drug delivery by triggering drug release in response to external stimuli, such as near-infrared (NIR) lasers [17–19].

In this study, a spray atomization technique was employed to fabricate a hydrogel composed of Ti_3C_2 MXene and SA loaded with ciprofloxacin (CIP). We evaluated the antibacterial properties and wound-healing capabilities of this hydrogel. Upon exposure to NIR radiation, the CIP-loaded MXene/SA hydrogel (CIP-MX@Gel) displayed outstanding photothermal conversion ability and maintained biocompatibility and antibacterial activity through controlled drug release. The CIP-MX@Gel system was developed to accelerate wound healing while inhibiting bacterial infections, perform rapid drug release via NIR, and carry out both functions. This intriguing approach could eventually be used in tissue engineering to achieve enhanced wound healing.

2. Materials and methods

2.1. Materials

Ti_3C_2 MXene flakes were purchased from Haydale Technologies Co., Ltd. (UK). Alginic acid, sodium salt, and calcium chloride (≥97 %) were purchased from Sigma-Aldrich. The disposable biopsy punch used in this study had a diameter of 6 mm and was obtained from Kai Industries Co. Isoflurane (Ifran, Hana Pharm. Co., Ltd.); this punch was used for anesthesia during the experiments. A Tegaderm Film (3 M 1624 W) and a Press-To-Seal silicone isolator (9 mm, P24743, Invitrogen, USA) were used for wound treatment. Deionized water (DW) was used to prepare the aqueous solutions.

2.2. Preparation of the MXene/SA and CIP-MXene/SA hydrogels (CIP-MX@Gel)

Ti_3C_2 MXene flakes (10 mg) were added to 70 % ethanol (10 mL) and centrifuged at 3000 rpm for 10 min. After removal of the supernatant, the MXene flakes were suspended in 10 mL of DW and sonicated for 30 min to yield a homogeneous MXene solution. The MXene solution was mixed with 2 wt% SA solution in a 1:1 ratio. Concurrently, $CaCl_2$ (4 g) was dissolved in 96 g of DW to create a 4 wt% $CaCl_2$ solution. Both solutions were individually transferred to 20 mL containers and sprayed. The mixed pre-hydrogel solution was cross-linked at room temperature for 10 min to prepare the hydrogel.

2.3. Characterization of the MXene/SA hydrogels (MX@Gel)

For scanning electron microscope (SEM) imaging, the MX@Gel was frozen at −80 °C for 6 h, and then dried overnight in a freeze-dryer. The samples were platinum coated for 80 s at 30 mA before imaging using a HITACHI (SU3800) scanning electron microscope at 15.0 kV. The captured images were then analyzed and quantified using ImageJ software. To assess the ultraviolet–visible (UV–vis) spectra and transmittance, 200 μL of the MXene/SA solution was dispensed in the lid of an Eppendorf tube. $CaCl_2$ was then sprayed onto the solution to induce hydrogel formation. The hydrogel was placed in a 48-well plate and measured using a TECAN (INFINITE 200) instrument. Fourier transform infrared spectroscopy (FTIR, JASCO FT/IR 4600) was performed using the MXene, CIP, and CIP-MXene (CIP-MX) samples. Transparent pellets were prepared by blending each sample with KBr and then compressing the mixture. The following formula was used to calculate the swelling ratio of the MX@Gel: $Swelling\ ratio = \frac{Ws-Wd}{Wd}$.

where Ws is the swelling weight and Wd is the dry weight of the fabricated MX@Gel.

2.4. Photothermal performance of the MX@Gels

To confirm the photothermal conversion of MXene, a NIR laser was positioned 5 cm above the prepared MX@Gel. After 10 min of irradiation, temperature changes within the hydrogel were continuously monitored using an infrared camera (FTIR-E5). The photothermal stability of the hydrogel was also assessed through cyclic NIR irradiation by toggling the laser on and off at 5-min intervals to calculate the temperature fluctuations. Furthermore, the impact of NIR laser density on the photothermal conversion efficiency of the MX@Gel was investigated by incrementally increasing the laser density in 0.5 W/cm^2 intervals. All temperature changes were tested at least three times, measured at 5-s intervals, and analyzed using ImageJ software.

2.5. Drug loading and release of the CIP-MX and CIP-MX@Gel

CIP solution was added dropwise to a 0.8 mg/mL MXene solution in a 1:1 ratio, and then stirred for 24 h in the dark. Subsequently, the mixture was separated via centrifugation at 4500 rpm for 30 min, and then subjected to three washes with DW to eliminate unbound CIP. The solution was then combined with SA. Finally, the desired CIP-MX@Gel was prepared by spraying the mixture with a $CaCl_2$ solution. UV–vis measurements were then conducted to validate the successful loading of CIP onto the MXene substrate. Each MXene, CIP, and CIP-MX solution (1 mL each) was individually placed in a 12.5 mm × 12.5 mm, 10 mm cuvette, and their absorbance was measured using a spectrophotometer (TECAN, INFINITE 200). To assess the drug release profile of CIP-MX@Gel with or without NIR irradiation, the hydrogel was immersed in 1 mL of DW, and the supernatant was collected at various time points. UV–vis measurements were performed to compare the absorbance levels before and after the release process.

2.6. Cell culture

Human dermal fibroblasts (HDFs) were cultured in Dulbecco's modified Eagle's medium (DMEM; Stemcell™) supplemented with 10 % fetal bovine serum and 1 % penicillin-streptomycin-glutamine (Gibco). Cells were cultured in a 37 °C, 5 % CO_2 incubator, with fresh medium replenished every 2–3 days.

2.7. Biocompatibility of the MX@Gel and CIP-MX@Gel

Each well of a 48-well cell culture plate was coated with 100 μL of MX@Gel. Subsequently, the cells were sterilized by UV irradiation for 10 min and washed with PBS. A total of 5×10^4 HDF cells per well were seeded onto the hydrogel surface. Cell viability was assessed every 3 days using a live/dead assay (Invitrogen, L3224) by calculating the ratio of live cells to the total cell count. A fluorescence microscope was used to

capture images for analysis.

2.8. In vitro MX@Gel and CIP-MX@Gel wound healing property

5×10^4 HDF cells were seeded in the lower chamber of the transwell® (37012, SPL). Once cell confluency reached 90 %, a scratch was created within the well using a 200 μL pipette tip for the scratch assay. Subsequently, hydrogels containing various concentrations of MXene were placed in the upper chambers of the Transwell® inserts. Images were then captured at 12 h intervals using a microscope.

2.9. Gene expression profile

Total RNAs were extracted from the cell using Trizol (Trizol®, Life Technology, USA) and reverse-transcribed into cDNA using the SuperScript Synthesis System (Invitrogen™, USA). Real-time PCR was performed using SYBR Green PCR Master-mix, according to the manufacturer's instructions for the ABI StepOnePlus™ real-time PCR system (Applied Biosystems, USA). cDNA samples were analyzed to detect the genes of interest (*MMP3*, *IL6*, *Col1a1*, and *Col3a1*), and *GAPDH* was employed as the reference gene. The gene expression level of each target was then calculated as $-2^{\Delta\Delta Ct}$ [20]. Each sample was analyzed at least three times to detect the gene of interest. Matrix metallopeptidase 3 (*MMP3*, Hs00968305_m1), collagen type III alpha 1 (*Col31*, Hs00943809_m1), collagen type I alpha 1 (*Cola1*, Hs01076777_m1), and interleukin (*IL6*, Hs00174131_m1) were selected as the target genes.

2.10. Antibacterial assay of the MX@Gel and CIP-MX@Gel

Agar plates were prepared for bacterial testing. First, 0.3 g of agarose (A8963) and 0.5 of Lysogeny Broth (LB) (244520, Difco) were placed in a flask. Thereafter, 20 mL of DW was added to the flask, and the mixture was dissolved via heating in an autoclave. An agar plate was prepared by pouring the solution into a Petri dish. Briefly, 5 mL of a 2.5 % LB solution was poured into a 14 mL test tube. *Escherichia coli* (*E. coli*) and *Staphylococcus aureus (S. aureus*) were respectively inoculated in the solution, and then the mixture was incubated in a 37 °C, 400 rpm shaking incubator for 24 h. After 100 μL of 1.85×10^8 CFU/mL of *E. coli* and 1.75×10^8 CFU/mL of *S. aureus* were inoculated on the agar plate, they were spread evenly on the agar plate with a spreader. The hydrogel prepared using the above method was placed on an agar plate inoculated with bacteria and incubated for 24 h in a 37 °C incubator. The zone of inhibition (ZOI) was then quantified and the number of bacterial colonies was determined using a spreader.

2.11. Animal experiments with the sprayable MX@Gel and CIP-MX@Gel on mice wounds

Animal experiments involved the application of sprayable MX@Gel to the wounds of mice. The Institutional Animal Care and Use Committee at Seoul National University approved the experimental protocols (SNU-230222-1-1). BALB/c-nu mice obtained from NARA Biotech (Republic of Korea) were used in this study. Full-thickness wounds were created using a biopsy punch with a diameter of 6 mm. An adhesive silicone isolator with a diameter of 9 mm was applied to the wounds to prevent natural wound contraction. Wound areas were normalized using this isolator. The silicone isolator was replaced with a new isolator every 3 or 4 days throughout the experimental period, and Tegaderm was used as a replacement in the sham group. On days 7 and 14, mice were euthanized using excess CO_2, and their skin was collected. After washing with PBS, the skin samples were fixed with 4 % paraformaldehyde (PFA).

2.12. Histological analysis

The wounds embedded in paraffin blocks were sectioned at a thickness of 5 μm. Hematoxylin and eosin (H&E) and Masson's trichrome (MTC) staining were performed to evaluate regenerated skin tissues. The panniculus gap and granulation tissue thickness were measured using ImageJ software, following a previously reported methodology [21]. The distance between the termini of the adipose tissues served as the measurement for the panniculus gap margin.

2.13. Immunohistochemistry

The skin tissue sections were deparaffinized, hydrated, and subjected to antigen retrieval for immunostaining. Thereafter, the sections were blocked for 1 h at room temperature using 5 % normal goat serum (S-1000-20, Vector Laboratories). The samples were incubated overnight at 4 °C with the primary antibodies: alpha smooth muscle actin (1:200, ab124964, Abcam) or CD31 (1:200, ab182981, Abcam). After washing with PBS, the sections were incubated with secondary antibodies (Abcam, Cambridge, UK) diluted in PBS for 1 h. Finally, the sections were mounted using a DAPI-containing mounting medium (ab104139) and observed under a fluorescence microscope (Ds-Qi2, Nikon).

2.14. Statistical analysis

Each experiment was conducted with at least three replicates. Data are presented as mean values and their respective standard deviations (SD). Statistical significance was assessed using one-way ANOVA.

3. Results

3.1. Preparation and characterization of the MXene/SA hydrogel (MX@Gel)

Sprayable hydrogels offer distinct advantages, including rapid hydrogel formation and immediate *in situ* action, making them convenient for the treatment of large wounds [22,23]. In preparation, various concentrations of MXene flakes were mixed with 2 wt% SA solution and 4 wt% $CaCl_2$ solution was prepared in a separate spray bottle for application (Fig. 1A, Fig. S1, and Movie S1). The SEM images revealed the surface morphology of the 2D MXene flakes (Fig. 1B). Elemental mapping analysis conducted using Energy Dispersive X-ray Spectroscopy (EDS) revealed the presence of Ti, O, F, C, and Cl, which are the main elements of Ti_3C_2 MXene, with Ti as the most abundant element (51.99 wt%; Fig. 1C). X-ray diffraction (XRD) analysis confirmed the presence of the (002) diffraction peak of Ti_3C_2 MXene (Fig. 1D). The UV–vis spectroscopy results for the MXene/SA solution revealed the UV absorption spectrum of MXene at 316 nm and that of SA at 265 nm (Fig. 1E). The MX@Gel was formulated with different concentrations of MXene (0, 10, 50, 100 μg/mL) in MXene/SA solution and $CaCl_2$ solution (Fig. 1F). As shown in Fig. 1G, as the MXene content increased, the swelling ratio of the MX@Gel gradually decreased, reaching 1798.62 % at 100 μg/mL. After lyophilization of the MX@Gel, the SEM image of the cross-sectioned hydrogel surface confirmed the presence of a porous structure (Fig. 1H and Fig. S1), and the size of the pores decreased as the MXene content increased (Fig. 1I). Remarkably, the UV–vis absorption spectrum of MX@Gel containing MXene displayed a unique absorption in the biological window region (750–850 nm) (Fig. 1J). Moreover, the transmittance decreased as the MXene content increased (Fig. 1K).

3.2. Photothermal conversion property of the CIP-loaded MXene/SA hydrogel (CIP-MX@Gel)

MXenes have demonstrated excellent photothermal conversion properties that are attributed to the localized surface plasmon resonance (LSPR) effect [24–26]. To evaluate the excellent photothermal

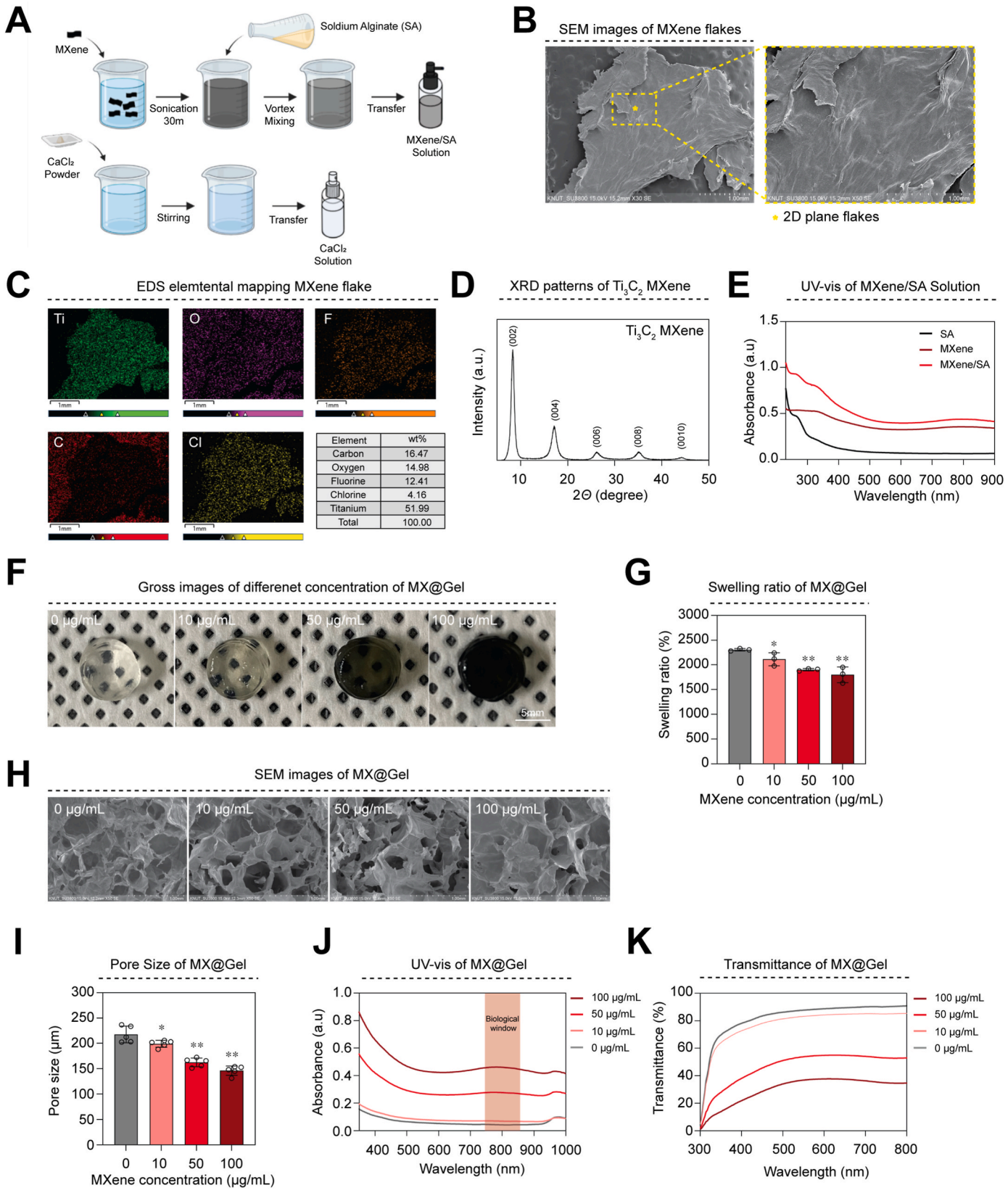

Fig. 1. Characterization of MXene and MXene/SA hydrogel (MX@Gel).A) Schematic diagram of the sprayable MX@Gel preparation process. Each spray contains MXene/SA solution and $CaCl_2$ solution. B) SEM image of MXene flakes. C) EDS mapping analysis of MXene flakes (green: Ti, purple: O, orange: F, red: C, yellow: Cl) and element ratios. D) XRD pattern of MXene flakes. E) UV–vis spectrum of MXene/SA solution. F) Gross images of MX@Gels fabricated with various MXene concentrations (0, 10, 50, 100 μg/mL). G) Swelling ratio of MX@Gel (n = 3). H) SEM images of MX@Gel. I) Pore size of MX@Gel (n = 5). J) UV–vis of MX@Gel. K) Transmittance of MXene/SA hydrogel. All data represent mean ± SD. *$p < 0.05$, **$p < 0.01$. The symbol * indicates comparisons with 0 μg/mL. Scale bars = 1 mm (B, C, H), 5 mm (F).

conversion properties of MXene remain in the hydrogel form, we investigated the photothermal efficiency of MX@Gel during 808 nm NIR irradiation (Fig. 2A, Fig. S2, and Movie S2). As the MXene concentration increased, the photothermal conversion efficiency also increased. At a concentration of 100 μg/mL, the temperature escalated to a maximum of 61.2 °C within 10 min.

To assess the stability of the photothermal conversion properties, we conducted a cyclic test on MX@Gel, in which repeated cycles of NIR on/off were performed. As shown in Fig. 2B, this iterative process revealed consistent and stable temperature fluctuations characterized by a rapid temperature increase during laser activation and a swift decrease upon deactivation. The photothermal conversion effect of MX@Gel could also be controlled by varying the laser density (0.50, 1.00, 1.50, 2.00 W/cm^2) (Fig. 2C and Fig. S3).

Combining the photothermal conversion effect of MXene with chemotherapy can precisely control drug release and improve treatment efficacy due to the heat generated by NIR [18,27]. The hydrophilic characteristics of MXene, adorned with functional groups, such as F, O, and OH-, and its negative surface charge facilitated rapid CIP loading through electrostatic attraction and hydrogen bonding. The drug-loading process involved sonication of the MXene dispersion, mixed CIP, and CIP-loaded MXene (CIP-MX) using a stirrer (Fig. 2D). The UV–vis absorption spectrum of MXene combined with CIP revealed a distinct 270 nm absorption peak for CIP, even after washing (Fig. 2E). FT-IR analysis confirmed drug loading, which was revealed by shifts in the characteristic peaks of MXene (-OH stretching, C═O, and –OH bending vibrations at 3440 cm^{-1}, 1633 cm$^{-1,}$ and 1383 cm^{-1}, respectively). The distinct peak of CIP is a C═O stretch of the carboxyl group at

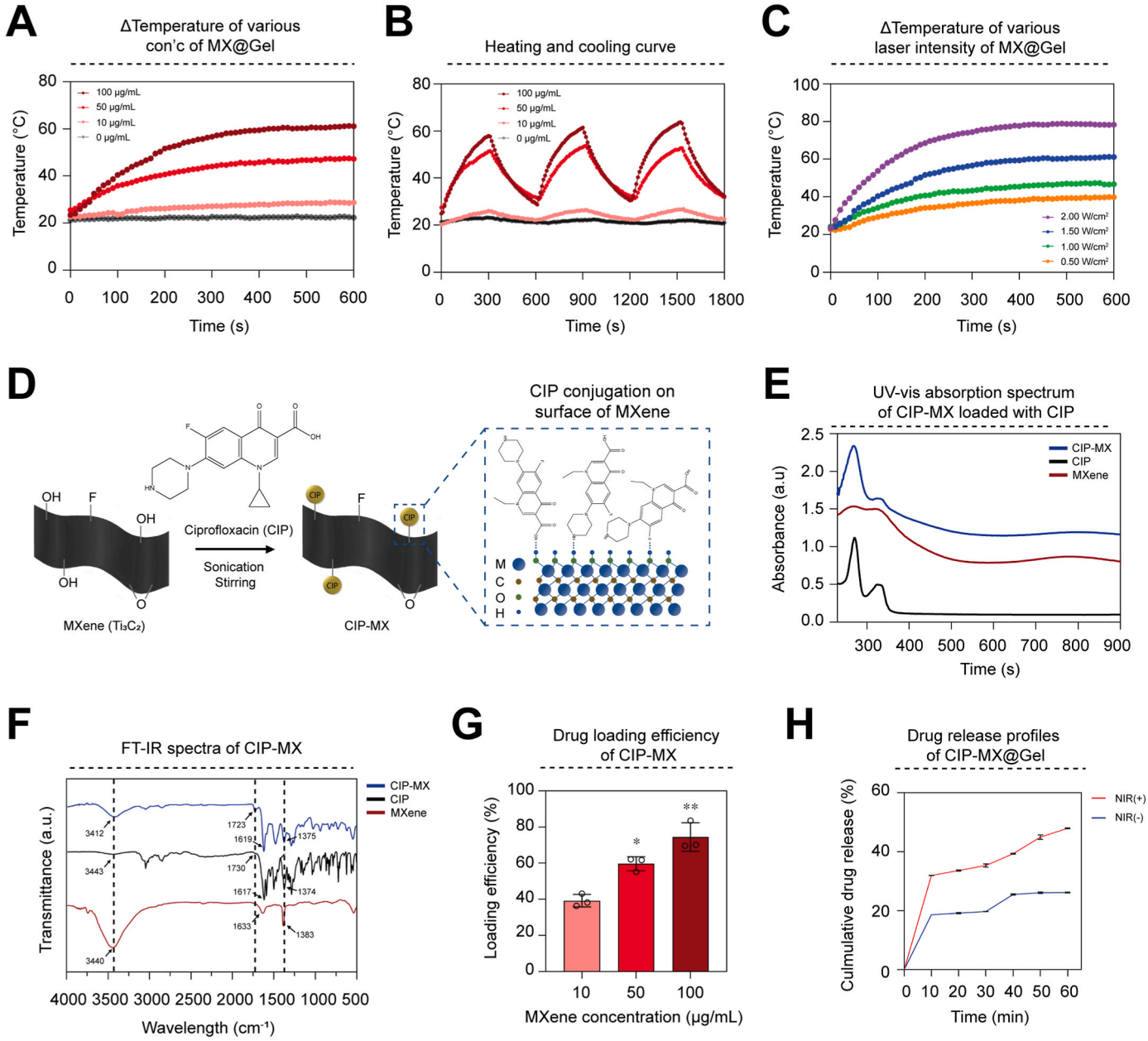

Fig. 2. Photothermal property and drug loading of MX@Gel.A) Temperature change of MX@Gel containing MXene at various concentrations (0, 10, 50, 100 μg/mL) under near-infrared (NIR) laser irradiation (808 nm, 0.5 W/cm^2). B) Heating and cooling curves of MX@Gel by laser on/off cycle. C) MX@Gel temperature change graph according to various laser densities (0.50, 1.00, 1.50, 2.00 W/cm^2). D) Schematic of loading ciprofloxacin on MXene surface. E) UV–vis absorption spectrum of CIP-loaded MXene (CIP-MX) F) FT-IR spectra of CIP-MX. G) Drug loading efficiency of CIP-MX (n = 3). H) CIP-loaded MXene/SA hydrogel (CIP-MX@Gel) drug release profiles under NIR laser irradiation. All data represent mean ± SD. *p < 0.05, **p < 0.01. The symbol * indicates comparisons with 10 μg/mL.

1730 cm^{-1}. The FT-IR spectrum of CIP-MX showed a shift in the peaks at 3412 cm^{-1} and 1723 cm^{-1}, corresponding to OH stretching and C═O, respectively, which is due to drug loading. This result indicates an interaction between the drug and MXene (Fig. 2F and Fig. S4). The loading efficiency of CIP increased with increasing MXene concentration (74 % at 100 μg/mL) (Fig. 2G). Upon NIR irradiation, the drug concentration released from CIP-MX@Gel containing 100 μg/mL concentration of MXene was approximately 1.7-fold higher, owing to the photothermal conversion effect (Fig. 2H).

3.3. Biocompatibility and cell migration of the CIP-MX@Gel with antibacterial property

Biocompatibility is essential for evaluating the safety of the interactions with living tissues [28,29]. To assess the biocompatibility of the MX@Gel, we seeded Human dermal fibroblasts (HDF) on the hydrogel and performed a live/dead assay (Fig. 3A). During the culture periods of 1, 4, and 7 days, cell viability was greater than 90 % in all groups (Fig. 3B).

Fibroblasts are one of the major cell types found in the skin tissue. Fibroblasts play an essential role in the wound healing process, such as collagen production and skin tissue remodeling [30,31]. A scratch assay was performed to determine the effect of the MX@Gel on the migration of HDF (Fig. 3C). Cell migration was recorded at 0, 12, and 24 h. The CIP-MX@Gel group displayed the highest cell migration rate (84.86 %) (Fig. 3D).

Fibroblasts produce enzymes called matrix metallopeptidases (MMPs) that break down the ECM during wound healing. MMP3 is a type of MMP involved in wound healing and tissue remodeling. MMP3 is necessary for the initiation of tissue reconstruction and its absence in mice delays wound healing [32,33]. In this study, the gene expression levels of *MMP3* and three ECM components, *Il6*, *Col3a1*, and *Col1a1*, were investigated in fibroblasts cultured on six different concentrations of MX@Gel: 0 μg/mL, 10 μg/mL, 50 μg/mL, 100 μg/mL, CIP-MX@Gel, and tissue culture polystyrene (TCP) (Fig. 3E). MMP3 expression was upregulated in fibroblasts cultured on all concentrations of MXene. However, 50 μg/mL MXene resulted in the most upregulated expression of fibroblasts after 24 h of culture. The prognosis and progression of a tissue state may be significantly affected by the upregulation or downregulation of collagen types, particularly Col I and III [34,35]. The gene expression of *Cola1* was higher in the groups comprising MXene than in the 0 μg/mL or TCP group. However, Col3a1 expression was downregulated in the MXene-treated and CIP-loaded groups. Interleukin (IL)-6 is a crucial modulator of inflammatory and reparative processes, and is involved in the differentiation, activation, and proliferation of leukocytes, endothelial cells, keratinocytes, and fibroblasts [36–38]. The gene expression of *IL-6* was high in the MXene and CIP-loaded groups. Expression was maintained at the same level until 24 h, and then decreased after 48 h of culture. These results suggest that the MXene nanoparticles accelerate dermal tissue reconstruction, thereby reducing scar formation this is because the upregulation of MMP3 expression is necessary for initiating tissue reconstruction and the downregulation of Col3a1 expression is associated with ECM degradation. The findings of this study are consistent with those of previous wound-healing studies, which have shown that groups comprising MXene can accelerate wound healing and tissue reconstruction.

To evaluate the wound-healing ability of CIP-MX@Gel using photothermal chemotherapy, we evaluated the antibacterial activity by irradiating MX@Gel with NIR in each group. The inhibition zone of CIP-MX@Gel against *E. coli* and *S. aureus* was identified using the disk diffusion method (Fig. 3F). No antibacterial effect was observed in the group without CIP loading. However, antibacterial activity was observed against *E. coli* and *S. aureus* in the group loaded with CIP alone. In particular, the NIR-irradiated group showed significantly greater bacterial inhibition than the non-NIR-irradiated group (Fig. 3G).

3.4. In vivo wound healing effect of CIP-MX@Gel in mice

We evaluated the *in vivo* wound healing effect of CIP-MX@Gel in mice by assessing its therapeutic efficacy in full-thickness skin wounds (Fig. 4A). Notably, the hydrogel was found to form well on the skin (Fig. S5). Mice were randomly assigned to six experimental groups: sham, 0 μg/mL, 100 μg/mL, 100 μg/mL w/NIR, CIP-MX@Gel, and CIP-MX@Gel w/NIR. To quantify the wound healing progress, we created a 6 mm diameter wound on the dorsal skin of mice and digitally captured wound images on days 0, 3, 7, 10, and 14. The wound area was calculated relative to the initial size on day 0. Fig. 4B and C illustrate the temporal changes in wound size in each group. Notably, the CIP-MX@Gel w/NIR group showed significantly accelerated wound healing compared to the other groups at all the examined time points. On day 7, the CIP-MX@Gel w/NIR group exhibited an impressive wound closure of 61.03 % (±5.60 %), and by day 14, wound closure reached 90.14 % (±2.31 %), indicating the fastest healing rate. In contrast, the other groups had comparatively slower wound healing: on day 14, the sham group achieved 77.41 % (±3.26 %), the 0 μg/mL group achieved 75.15 % (±2.61 %), the 100 μg/mL group achieved 53.07 % (±7.80 %), the 100 μg/mL w/NIR group achieved 50.93 % (±10.73 %), and the CIP-MX@Gel w/NIR group achieved 85.74 % (±5.71 %) wound closure. Furthermore, we conducted histological evaluation of the wounds using tissue samples collected on days 7 and 14 (Fig. 4E). Hematoxylin-Eosin (H&E) staining revealed that the panniculus gap on day 7 was significantly shorter in the CIP-MX@Gel w/NIR group than that in the other groups (Fig. 4F). Additionally, the CIP-MX@Gel w/NIR group displayed the highest granulation threshold on day 7 (Fig. 4H), indicating enhanced tissue regeneration. Consistent with the trends observed on day 7 (Fig. 4G and I), the CIP-MX@Gel w/NIR group maintained the shortest panniculus gap and thickest granulation threshold on day 14. Statistical analysis revealed a significant reduction in the panniculus gap of the CIP-MX@Gel w/NIR group compared to that of the other groups. Masson's trichrome (MTC) staining was performed on days 7 and 14 (Fig. 5A). Consistently, the results revealed that the CIP-MX@Gel w/NIR group exhibited the highest abundance of collagen fibers compared to the other groups, as found on days 7 and 14 (Fig. 5B and C). These results suggest that the tissue regenerated in the CIP-MX@Gel w/NIR group closely resembles an intact, uninjured skin structure.

The immunofluorescence staining results of α-smooth muscle actin (α-SMA) and CD31 in wound samples on day 14 are presented in Fig. 5D. These results were used to explore the potential activation of angiogenic responses *in vivo* wounds. Minimal positive staining was observed in the sham and 0 μg/mL groups. Quantification of α-SMA and CD31 fluorescence intensity is shown in Fig. 5E and F. The CIP-MX@Gel w/NIR group exhibited more than 38 vessels, a significantly higher count than the other five groups. The CIP-MX@Gel group displayed approximately 15 vessels, whereas the sham and 0 μg/mL groups exhibited negligible vessel formation. These findings highlight the substantial role of CIP-MX@Gel w/NIR treatment in promoting wound healing and its potential as a promising therapeutic strategy for enhancing *in vivo* wound repair.

4. Discussion

The present study aimed to explore the potential of MXene-based hydrogel systems for enhancing wound healing and preventing bacterial infections. Incorporating MXenes into a hydrogel formulation is an advantageous strategy for drug delivery and photothermal conversion. Photothermal conversion is observed in many nanomaterials, including metallic nanostructures, semiconductors, carbon-based nanomaterials, organic polymers, two-dimensional (2D) transition metal carbides/nitrides (MXenes), and their hybrids [39]. Among them, MXene is a characteristic two-dimensional nanomaterial that has a typical layered structure and can be competitive with other photothermal materials. It has the highest specific surface area compared to 0-dimensional (0D),

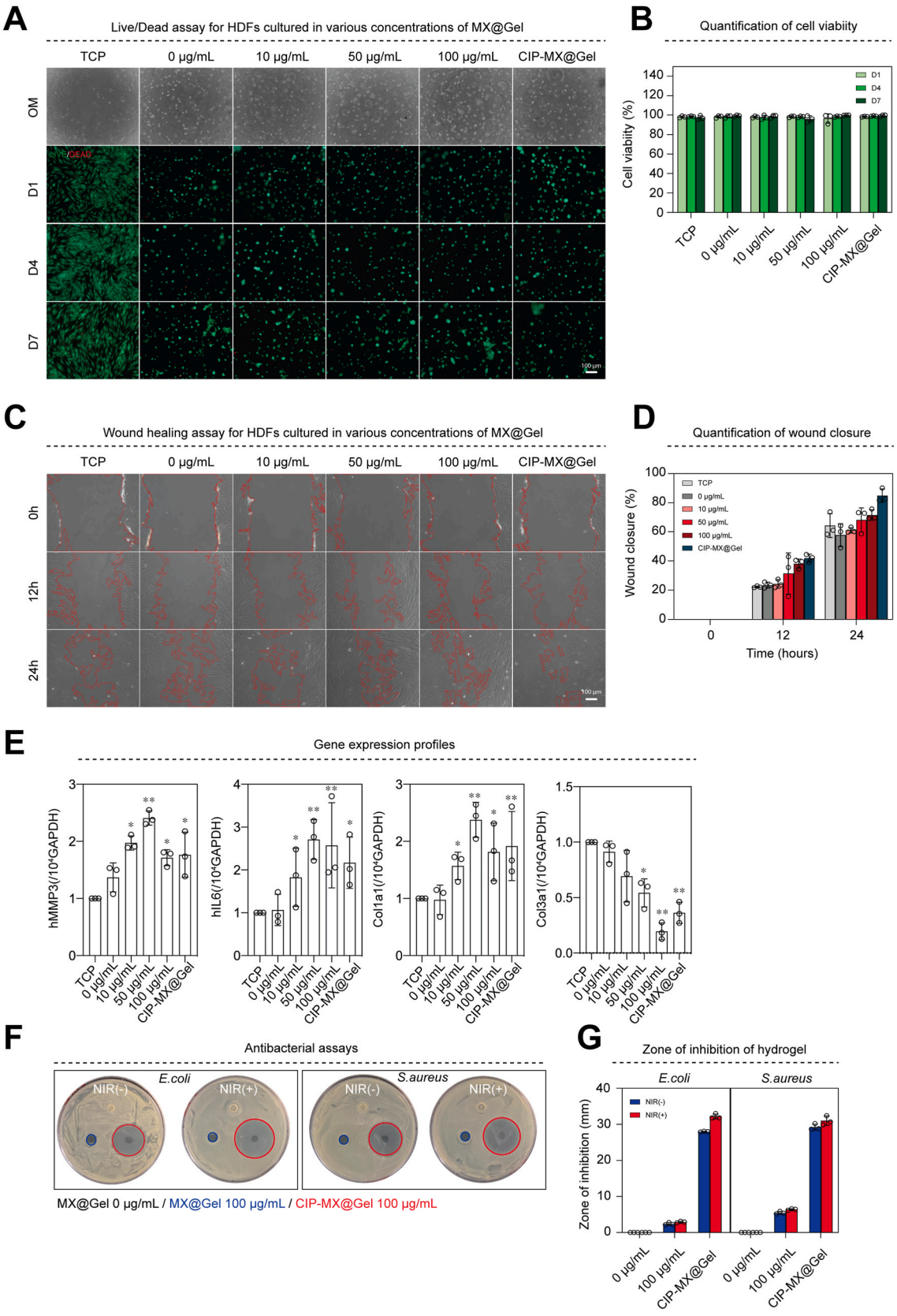

Fig. 3. Biocompatibility, cell migration and antibacterial properties of CIP-MX@Gel.A) Optical microscopy and Live/dead staining images of human dermal fibroblasts cultured on MX@Gel at 1, 4, and 7 days. B) quantification of cell viability of MX@Gels. C) Wound healing scratch assay of MX@Gel at different concentrations. D) Quantification of cell migration (n = 3). E) Gene expression profiles of MX@Gels (n = 3). F) Antibacterial gross images of *E. coli* and *S. aureus* in CIP-MX@Gel using smear plate method. G) Quantification of the zone of inhibition of CIP-MX@Gel (n = 3). All data represent mean ± SD. *p < 0.05, **p < 0.01. The symbol * indicates comparisons with 0 μg/mL. Scale bars = 100 μm (A, C).

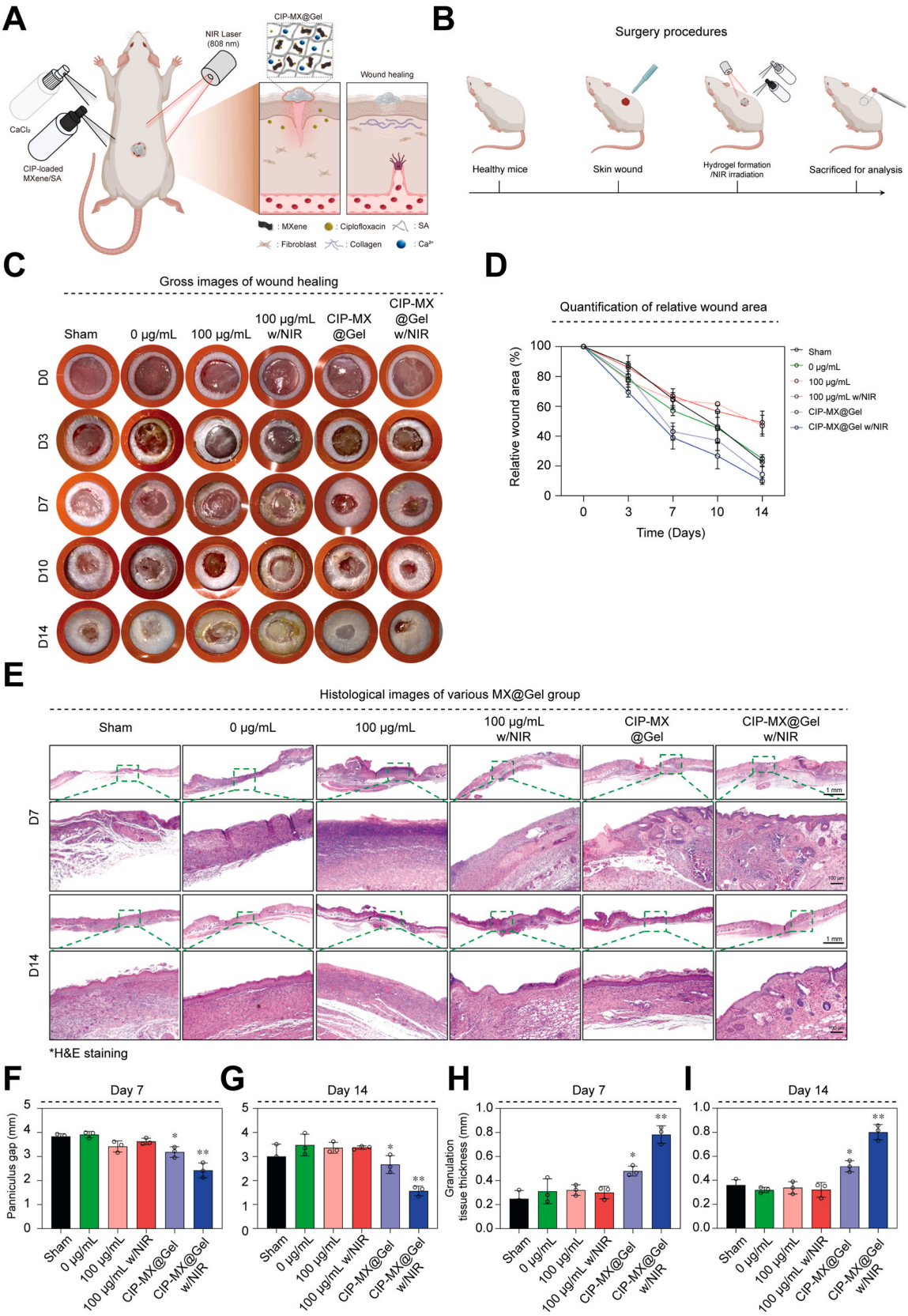

Fig. 4. *In vivo* wound healing assessment of CIP-MX@Gel.A) Schematic diagram of the formation process of sprayable CIP-MX@Gel, and drug release by NIR irradiation B) Schematic diagram of the experimental healing process *in vivo*. C) Wound images at days 0, 3, 7, 10 and 14 (Silicone isolator diameter = 9 mm). D) quantification of relative wound area. ($n \geq 3$) E) Hematoxylin and eosin (H&E) staining images on day 7 and 14 of wound tissues treated in different groups. F, G) Quantification of the panniculus gap at day 7 and day 14 in wound tissue treated with different groups. H, I) Quantification of the granulation tissue thickness at day 7 and day 14 in wound tissue treated with different groups. All data represent mean ± SD. *$p < 0.05$, **$p < 0.01$. The symbol * indicates comparisons with Sham. Scale bars = 1 mm (E), 100 μm (magnified images, E).

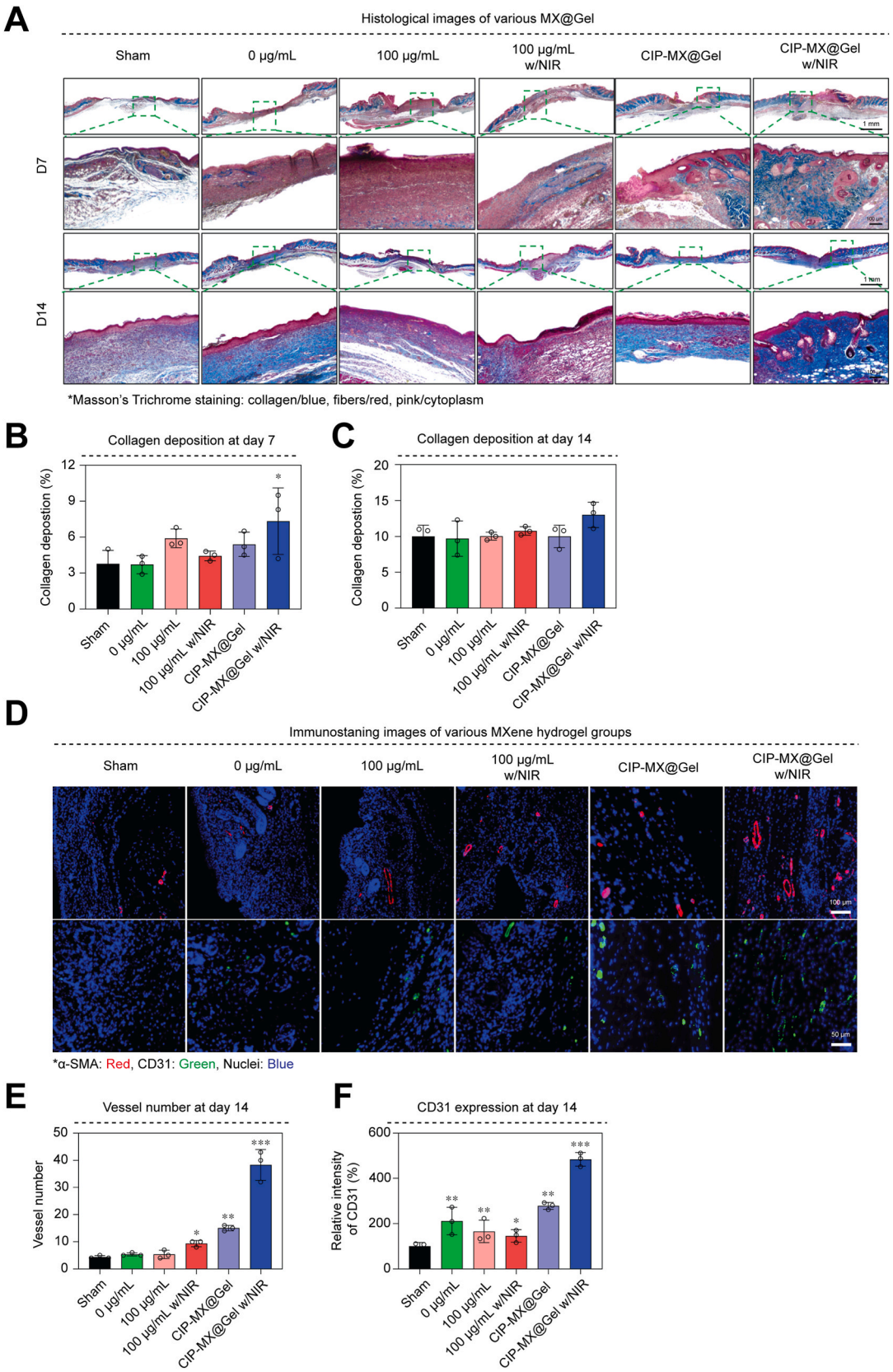

Fig. 5. CIP-MX@Gel accelerates wound healing in a mouse model.A) Masson's trichrome (MT) staining images on day 7 and 14 of wound tissues treated in different groups. B, C) Quantification of the collagen deposition at day 7 and day 14 in wound tissue treated with different groups. D) Immunohistochemistry staining image at day 14 in wound tissue treated with different groups. E) Quantification of the vessel number. F) Quantification of the relative intensity of CD31. All data represent mean ± SD. *$p < 0.05$, **$p < 0.01$, ***$p < 0.001$. The symbol * indicates comparisons with Sham. Scale bars = 1 mm (A), 100 μm (magnified images, A), 100 μm (α-SMA, D), 50 μm (CD31, D).

1-dimensional (1D), and bulk materials, so it responds quickly to light. Additionally, it can provide excellent in-plane electron mobility [40]. In particular, compared to graphene, one of the representative two-dimensional materials, various functional groups such as oxygen (-O), fluorine (-F), and hydroxyl group (-OH) exist on the surface of MXene, so it is well dispersed in polar solvents and provides surface functionalization. makes it possible and further increases its usability [41,42]. These unique properties of MXene, including its high surface area and tunable surface chemistry, enabled efficient loading and sustained release of CIP. Moreover, flakes of MXene are easily oxidized in both moist air and water. Due to its chemical instability, MXene may not be suitable for applications requiring long-term operation or ambient environments. However, in our system, the number of oxidation-accessible sites in the MXene flakes that can react with water is decreased when CIP interacts sufficiently with the MXene surface (Fig. 2D). It eventually stops MXene from oxidizing in the hydrogel. As a results, the high drug-loading capacity of the MXene/SA hydrogel (MX@Gel) system ensured the controlled and maintained release of CIP over time, which is critical for promoting wound healing and inhibiting bacterial growth. Notably, the exceptional photothermal conversion ability of MXenes enables precise spatial and temporal control of drug release via NIR stimulation [43]. By modulating MXene concentration and laser density, we demonstrated the proficiency of the MX@Gel in finely tuning its photothermal effect. This harmonious combination of photothermal conversion and drug delivery presents a promising avenue for overcoming the inherent limitations of conventional drug delivery systems [44,45].

The antibacterial activity of the CIP-MXene/SA hydrogel (CIP-MX@Gel) was assessed using drug release studies. The CIP-MX@Gel efficiently inhibited bacterial growth, which is of paramount importance in wound healing. Bacterial infections can significantly impede the wound healing process, and the ability of the hydrogel to release CIP in a controlled manner helps prevent infections at the wound site [46,47]. Furthermore, the excellent biocompatibility of the CIP-MX@Gel ensures that the hydrogel system is safe for application in the wound area.

The combination of controlled drug release and photothermal conversion in the CIP-MX@Gel system offers numerous advantages over traditional wound dressings. Hydrogels can create an optimal microenvironment for promoting tissue regeneration and accelerating wound healing by providing localized and sustained drug release. Additionally, the ability to trigger drug release through NIR stimulation enables on-demand drug delivery, which could be particularly useful in cases of wound infection or delayed healing [47–49].

Some challenges must be addressed in future studies. The drug-release profile must be optimized to achieve an ideal balance between promoting wound healing and antibacterial activity. Fine-tuning the hydrogel composition and drug-loading process may further enhance the therapeutic efficacy and long-term stability of MXene-based drug delivery systems.

Biocompatibility assessments confirmed the safety of the CIP-MX@Gels. Nuanced evaluation of HDF viability indicated excellent biocompatibility, suggesting a favorable safety profile for clinical applications. Moreover, the acceleration of fibroblast migration in the presence of the hydrogel underscores its potential to expedite wound healing at the cellular level.

The multifaceted attributes of the MXene-based hydrogel system were validated using *in vivo* experiments. Efficacy assessments using a murine model revealed accelerated wound closure and pronounced tissue regeneration in the presence of the CIP-MX@Gel. Enhanced granulation thresholds, augmented collagen fiber density, and increased angiogenic responses collectively underline the potential of this platform to holistically expedite wound healing. Overall, this study highlights the promising potential of MXene-based hydrogel systems for enhancing wound healing and preventing bacterial infections. CIP-MX@Gel demonstrated efficient drug delivery, excellent photothermal conversion ability, and antibacterial properties, making it a promising candidate for advanced wound care applications. CIP-MX@Gel could pave the way for innovative and effective tissue engineering and wound-healing therapies.

5. Conclusions

We successfully developed a controllable drug release system using the excellent photothermal conversion of MXene in a CIP-loaded MXene/SA hydrogel (CIP-MX@Gel). This sprayable hydrogel demonstrated rapid wound coverage, with instant formation upon application. In addition, the photothermal conversion efficiency of CIP-MX@Gel could be controlled by varying the MXene concentration and NIR laser density. The biocompatibility of this hydrogel, coupled with the antibacterial properties of CIP, showed remarkable wound-healing capabilities in both *in vitro* and *in vivo* studies. Collectively, these findings highlight the significant potential of CIP-MX@Gel for advancing chemo-photothermal therapy applications.

Funding sources

This work was supported by the Ministry of Science and ICT of Korea (NRF-2021R1C1C2004576). This research was also supported by the Korean Fund for Regenerative Medicine (KFRM) grant funded by the Korean government (the Ministry of Science and ICT and the Ministry of Health & Welfare of Korea). (Code: KFRM 22A0105L1-11).

CRediT authorship contribution statement

Hyeongtaek Park: Investigation, Methodology, Writing - original draft. **Jeong-Uk Kim:** Investigation, Methodology, Writing - original draft. **Soojin Kim:** Investigation, Methodology. **Nathaniel S. Hwang:** Supervision. **Hwan D. Kim:** Conceptualization, Investigation, Methodology, Supervision, Writing - original draft, Writing - review & editing.

Declaration of competing interest

The authors declare that they have no known competing financial interests or personal relationships that could have appeared to influence the work reported in this paper.

Data availability

Data will be made available on request.

Appendix A. Supplementary data

Supplementary data to this article can be found online at https://doi.org/10.1016/j.mtbio.2023.100881.

References

[1] H. Sorg, D.J. Tilkorn, S. Hager, J. Hauser, U. Mirastschijski, Skin wound healing: an update on the current knowledge and concepts, Eur. Surg. Res. 58 (1–2) (2016) 81–94.
[2] E.M. Tottoli, R. Dorati, I. Genta, E. Chiesa, S. Pisani, B. Conti, Skin wound healing process and new emerging Technologies for skin wound care and regeneration, Pharmaceutics 12 (8) (2020) 735.
[3] Y. Liang, J. He, B. Guo, Functional hydrogels as wound dressing to enhance wound healing, ACS Nano 15 (8) (2021) 12687–12722.
[4] H.S. Kim, X. Sun, J.-H. Lee, H.-W. Kim, X. Fu, K.W. Leong, Advanced drug delivery systems and artificial skin grafts for skin wound healing, Adv. Drug Deliv. Rev. 146 (2019) 209–239.
[5] S. Matoori, A. Veves, D.J. Mooney, Advanced bandages for diabetic wound healing, Sci. Transl. Med. 13 (585) (2021), eabe4839.
[6] M. Soleimanpour, S.S. Mirhaji, S. Jafari, H. Derakhshankhah, F. Mamashli, H. Nedaei, M.R. Karimi, H. Motasadizadeh, Y. Fatahi, A. Ghasemi, M. S. Nezamtaheri, M. Khajezade, M. Teimouri, B. Goliaei, C. Delattre, A.A. Saboury, Designing a new alginate-fibrinogen biomaterial composite hydrogel for wound healing, Sci. Rep. 12 (1) (2022) 7213.

[7] S. Cheng, H. Wang, X. Pan, C. Zhang, K. Zhang, Z. Chen, W. Dong, A. Xie, X. Qi, Dendritic hydrogels with robust inherent antibacterial properties for promoting bacteria-infected wound healing, ACS Appl. Mater. Interfaces 14 (9) (2022) 11144–11155.
[8] M. Morey, A. Pandit, Responsive triggering systems for delivery in chronic wound healing, Adv. Drug Deliv. Rev. 129 (2018) 169–193.
[9] Y.-H. An, J. Lee, D.U. Son, D.H. Kang, M.J. Park, K.W. Cho, S. Kim, S.-H. Kim, J. Ko, M.-H. Jang, J.Y. Lee, D.-H. Kim, N.S. Hwang, Facilitated transdermal drug delivery using nanocarriers-embedded electroconductive hydrogel coupled with reverse electrodialysis-driven iontophoresis, ACS Nano 14 (4) (2020) 4523–4535.
[10] N. Kalai Selvan, T.S. Shanmugarajan, V.N.V.A. Uppuluri, Hydrogel based scaffolding polymeric biomaterials: approaches towards skin tissue regeneration, J. Drug Deliv. Sci. Technol. 55 (2020), 101456.
[11] M. Li, Y. Liang, J. He, H. Zhang, B. Guo, Two-pronged strategy of biomechanically active and biochemically multifunctional hydrogel wound dressing to accelerate wound closure and wound healing, Chem. Mater. 32 (23) (2020) 9937–9953.
[12] M. Bahadoran, A. Shamloo, Y.D. Nokoorani, Development of a polyvinyl alcohol/sodium alginate hydrogel-based scaffold incorporating bFGF-encapsulated microspheres for accelerated wound healing, Sci. Rep. 10 (1) (2020) 7342.
[13] G.-W. Oh, S.-C. Kim, T.-H. Kim, W.-K. Jung, Characterization of an oxidized alginate-gelatin hydrogel incorporating a COS-salicylic acid conjugate for wound healing, Carbohydr. Polym. 252 (2021), 117145.
[14] M. Zhang, X. Qiao, W. Han, T. Jiang, F. Liu, X. Zhao, Alginate-chitosan oligosaccharide-ZnO composite hydrogel for accelerating wound healing, Carbohydr. Polym. 266 (2021), 118100.
[15] S.M. George, B. Kandasubramanian, Advancements in MXene-Polymer composites for various biomedical applications, Ceram. Int. 46 (7) (2020) 8522–8535.
[16] A. Zamhuri, G.P. Lim, N.L. Ma, K.S. Tee, C.F. Soon, MXene in the lens of biomedical engineering: synthesis, applications and future outlook, Biomed. Eng. Online 20 (1) (2021) 33.
[17] X. Han, J. Huang, H. Lin, Z. Wang, P. Li, Y. Chen, 2D ultrathin MXene-based drug-delivery nanoplatform for synergistic photothermal ablation and chemotherapy of cancer, Adv. Healthcare Mater. 7 (9) (2018), 1701394.
[18] L. Jin, X. Guo, D. Gao, C. Wu, B. Hu, G. Tan, N. Du, X. Cai, Z. Yang, X. Zhang, NIR-responsive MXene nanobelts for wound healing, NPG Asia Mater. 13 (1) (2021) 24.
[19] X. Yang, C. Zhang, D. Deng, Y. Gu, H. Wang, Q. Zhong, Multiple stimuli-responsive MXene-based hydrogel as intelligent drug delivery carriers for deep chronic wound healing, Small 18 (5) (2022), 2104368.
[20] K.J. Livak, T.D. Schmittgen, Analysis of relative gene expression data using real-time quantitative PCR and the 2−ΔΔCT method, Methods 25 (4) (2001) 402–408.
[21] Y.-H. An, D.H. Kim, E.J. Lee, D. Lee, M.J. Park, J. Ko, D.W. Kim, J. Koh, H.S. Hong, Y. Son, J.-Y. Cho, J.-U. Park, S.-D. Kim, N.S. Hwang, High-efficient production of adipose-derived stem cell (ADSC) secretome through maturation process and its non-scarring wound healing applications, Front. Bioeng. Biotechnol. 9 (2021).
[22] H. Geng, Q. Dai, H. Sun, L. Zhuang, A. Song, F. Caruso, J. Hao, J. Cui, Injectable and sprayable polyphenol-based hydrogels for controlling hemostasis, ACS Appl. Bio Mater. 3 (2) (2020) 1258–1266.
[23] Y. Liao, L. Xie, J. Ye, T. Chen, T. Huang, L. Shi, M. Yuan, Sprayable hydrogel for biomedical applications, Biomater. Sci. 10 (11) (2022) 2759–2771.
[24] H. Lin, X. Wang, L. Yu, Y. Chen, J. Shi, Two-dimensional ultrathin MXene ceramic nanosheets for photothermal conversion, Nano Lett. 17 (1) (2017) 384–391.
[25] D. Xu, Z. Li, L. Li, J. Wang, Insights into the photothermal conversion of 2D MXene nanomaterials: synthesis, mechanism, and applications, Adv. Funct. Mater. 30 (47) (2020), 2000712.
[26] Y. Zhang, W. Wang, J. Xie, K. Dai, F. Zhang, Q. Zheng, Smart and flexible CNTs@MXene heterostructure-decorated cellulose films with excellent electrothermal/photothermal conversion and EMI shielding performances, Carbon 200 (2022) 491–499.
[27] Y. Dong, S. Li, X. Li, X. Wang, Smart MXene/agarose hydrogel with photothermal property for controlled drug release, Int. J. Biol. Macromol. 190 (2021) 693–699.
[28] S. Naahidi, M. Jafari, M. Logan, Y. Wang, Y. Yuan, H. Bae, B. Dixon, P. Chen, Biocompatibility of hydrogel-based scaffolds for tissue engineering applications, Biotechnol. Adv. 35 (5) (2017) 530–544.
[29] H. Hu, X. Zhai, W. Li, S. Ji, W. Dong, W. Chen, W. Wei, Z. Lu, A photo-triggering double cross-linked adhesive, antibacterial, and biocompatible hydrogel for wound healing, iScience 25 (7) (2022).
[30] M. Schäfer, S. Werner, Transcriptional control of wound repair, Annu. Rev. Cell Dev. Biol. 23 (2007) 69–92.
[31] Y.H. Song, Y.T. Zhu, J. Ding, F.Y. Zhou, J.X. Xue, J.H. Jung, Z.J. Li, W.Y. Gao, Distribution of fibroblast growth factors and their roles in skin fibroblast cell migration, Mol. Med. Rep. 14 (4) (2016) 3336–3342.
[32] S.J.M. Yussof, E. Omar, D.R. Pai, S. Sood, Cellular events and biomarkers of wound healing, Indian J. Plast. Surg. 45 (2) (2012) 220–228.
[33] D.T.A. Ploeger, N.A. Hosper, M. Schipper, J.A. Koerts, S. de Rond, R.A. Bank, Cell plasticity in wound healing: paracrine factors of M1/M2 polarized macrophages influence the phenotypical state of dermal fibroblasts, Cell Commun. Signal. 11 (1) (2013) 29.
[34] W. Zhang, X. Bai, B. Zhao, Y. Li, Y. Zhang, Z. Li, X. Wang, L. Luo, F. Han, J. Zhang, S. Han, W. Cai, L. Su, K. Tao, J. Shi, D. Hu, Cell-free therapy based on adipose tissue stem cell-derived exosomes promotes wound healing via the PI3K/Akt signaling pathway, Exp. Cell Res. 370 (2) (2018) 333–342.
[35] A.L. Moore, C.D. Marshall, L.A. Barnes, M.P. Murphy, R.C. Ransom, M.T. Longaker, Scarless wound healing: transitioning from fetal research to regenerative healing, WIREs Developmental Biology 7 (2) (2018) e309.
[36] S. Akira, T. Hirano, T. Taga, T. Kishimoto, Biology of multifunctional cytokines: IL 6 and related molecules (IL 1 and TNF), Faseb. J. 4 (11) (1990) 2860–2867.
[37] M. Mihara, M. Hashizume, H. Yoshida, M. Suzuki, M. Shiina, IL-6/IL-6 receptor system and its role in physiological and pathological conditions, Clin. Sci. 122 (4) (2011) 143–159.
[38] B.Z. Johnson, A.W. Stevenson, C.M. Prêle, M.W. Fear, F.M. Wood, The role of IL-6 in skin fibrosis and cutaneous wound healing, Biomedicines 8 (5) (2020) 101.
[39] H. Ma, M. Xue, Recent advances in the photothermal applications of two-dimensional nanomaterials: photothermal therapy and beyond, J. Mater. Chem. A 9 (33) (2021) 17569–17591.
[40] X. Cui, Q. Ruan, X. Zhuo, X. Xia, J. Hu, R. Fu, Y. Li, J. Wang, H. Xu, Photothermal nanomaterials: a powerful light-to-heat converter, Chem. Rev. 123 (11) (2023) 6891–6952.
[41] M. Mozafari, M. Soroush, Surface functionalization of MXenes, Materials Advances 2 (22) (2021) 7277–7307.
[42] M. Peng, M. Dong, W. Wei, H. Xu, C. Liu, C. Shen, The introduction of amino termination on Ti3C2 MXene surface for its flexible film with excellent property, Carbon 179 (2021) 400–407.
[43] A. Liu, Y. Liu, G. Liu, A. Zhang, Y. Cheng, Y. Li, L. Zhang, L. Wang, H. Zhou, J. Liu, H. Wang, Engineering of surface modified Ti3C2Tx MXene based dually controlled drug release system for synergistic multitherapies of cancer, Chem. Eng. J. 448 (2022), 137691.
[44] J. Yang, D. Shen, L. Zhou, W. Li, X. Li, C. Yao, R. Wang, A.M. El-Toni, F. Zhang, D. Zhao, Spatially confined fabrication of core–shell gold Nanocages@Mesoporous silica for near-infrared controlled photothermal drug release, Chem. Mater. 25 (15) (2013) 3030–3037.
[45] K.J. Rambhia, P.X. Ma, Controlled drug release for tissue engineering, J. Contr. Release 219 (2015) 119–128.
[46] M. Suhaeri, M.H. Noh, J.H. Moon, I.G. Kim, S.J. Oh, S.S. Ha, J.H. Lee, K. Park, Novel skin patch combining human fibroblast-derived matrix and ciprofloxacin for infected wound healing, Theranostics 8 (18) (2018) 5025–5038.
[47] W.-L. Chiang, T.-T. Lin, R. Sureshbabu, W.-T. Chia, H.-C. Hsiao, H.-Y. Liu, C.-M. Yang, H.-W. Sung, A rapid drug release system with a NIR light-activated molecular switch for dual-modality photothermal/antibiotic treatments of subcutaneous abscesses, J. Contr. Release 199 (2015) 53–62.
[48] Y. Sun, J. Liu, H. Wang, S. Li, X. Pan, B. Xu, H. Yang, Q. Wu, W. Li, X. Su, Z. Huang, X. Guo, H. Liu, NIR laser-triggered microneedle-based liquid band-aid for wound care, Adv. Funct. Mater. 31 (29) (2021), 2100218.
[49] S. Wang, Z. Zhang, S. Wei, F. He, Z. Li, H.-H. Wang, Y. Huang, Z. Nie, Near-infrared light-controllable MXene hydrogel for tunable on-demand release of therapeutic proteins, Acta Biomater. 130 (2021) 138–148.